



Experimental insights into adhesion and friction between nominally dry rough surfaces

Bart Weber,^{*}¹ Julien Scheibert,¹ Maarten P. de Boer,¹ and Ali Dhinojwala¹

Adhesion and friction between solids in ambient air control applications such as precision positioning and traction of tires. For all practical surfaces, the interfaces between solids are rough. Contact occurs at nano- or micro-contact junctions and the contact area of these junctions changes upon normal or shear loading and during sliding. The multiscale roughness, material parameters such as interfacial bonding, mechanical properties, sliding velocity, and normal load all contribute to adhesion and friction, resulting in diverse phenomena. Here, we highlight four recent advances relevant to materials ranging from ceramics to elastomers. They elucidate the importance of real contact area for soft and hard materials and of rate-state-friction models for explaining the transition from stick-slip to steady sliding for hard contacts. We also outline some remaining open experimental challenges related to friction and adhesion of dry multi-contact interfaces.

Introduction

Unlubricated rough contact interfaces are ubiquitous in nature and in industrial applications and involve a variety of materials with different properties and length scales of roughness. For example, the “soft” finger-on-touchscreen contact through which we communicate with the digital world is controlled by the topography of our fingers and viscoelastic tissue mechanics, under moderate few-MPa pressures.^{1–3} In contrast, the “hard” contacts that play a role in microelectromechanical systems (MEMS) involve few-GPa pressures and very small real contact area, as compared to the apparent contact area.^{4,5} Understanding adhesion and friction of these complex interfaces remains a formidable challenge.⁶ However, this understanding will help design better traction for tires,⁷ reversible adhesives for biomedical applications inspired by geckos,^{8,9} and can help in explaining how friction controls avalanches and earthquakes.¹⁰

Figure 1 shows a contact of two solid surfaces under an applied normal load, resulting in a multi-contact interface. For hard-hard surfaces the actual contact area is much smaller than the projected area and the true contact area increases slowly with normal load, due to elastoplastic deformation of

contact junctions. In the case of soft materials, one can achieve near conformal contact using modest normal loads, leading to substantial adhesion and friction.

Although friction and adhesion both originate from the same intermolecular forces, no common framework is yet available to describe them at the macroscale. Initially driven by the earthquake science community, comprehensive, although empirical laws for macroscopic friction are now widely accepted. These constitute the so-called rate-and-state friction laws. As reviewed in Reference 11, they rely on a decomposition of the friction force as a product of the real contact area and the friction strength of the interface. The latter is expected to depend on the sliding velocity (rate effect), whereas the former incorporates not only the combined effects of normal load and surface roughness, but also the increase in area as contact time increases (aging/state effect). The detailed morphology of the real contact controls most macroscopic responses, including pull-off forces, dynamic and static friction forces, wear, thermal and electrical conductivity, and the ability to seal against leakage. The associated micro- or nano-junctions are the regions where all of the mechanical stress is concentrated and can lead to plastic deformation, physico-chemical aging,^{12,13} capillary

Bart Weber, Advanced Research Center for Nanolithography (ARCNL), Amsterdam, The Netherlands; Van der Waals-Zeeman Institute, Institute of Physics, University of Amsterdam, Amsterdam, The Netherlands; b.weber@arcnl.nl

Julien Scheibert, Univ Lyon, Ecole Centrale de Lyon, ENISE, ENTPE, CNRS, Laboratoire de Tribologie et Dynamique des Systèmes LTDS, UMR 5513, Ecully, France; julien.scheibert@cnrs.fr

Maarten P. de Boer, Mechanical Engineering, Carnegie Mellon University, Pittsburgh, USA; mpdebo@andrew.cmu.edu

Ali Dhinojwala, School of Polymer Science and Polymer Engineering, The University of Akron, Akron, USA; ali4@uakron.edu

^{*}Corresponding author

doi:10.1557/s43577-022-00464-6

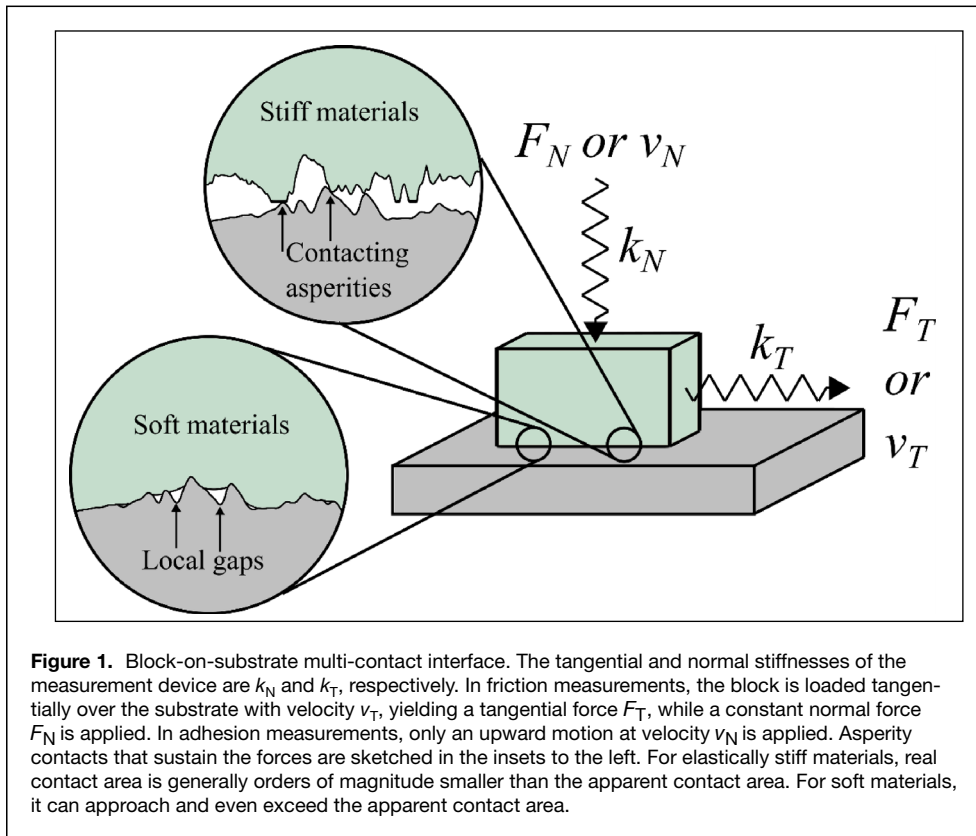


Figure 1. Block-on-substrate multi-contact interface. The tangential and normal stiffnesses of the measurement device are k_N and k_T , respectively. In friction measurements, the block is loaded tangentially over the substrate with velocity v_T , yielding a tangential force F_T , while a constant normal force F_N is applied. In adhesion measurements, only an upward motion at velocity v_N is applied. Asperity contacts that sustain the forces are sketched in the insets to the left. For elastically stiff materials, real contact area is generally orders of magnitude smaller than the apparent contact area. For soft materials, it can approach and even exceed the apparent contact area.

The scope of this article is to illustrate, through specific examples, some recent innovative experiments performed on dry rough contact interfaces, and the insights they provided into the adhesion and friction of such systems. In the first case study, we present MEMS-based adhesion and friction measurements at stiff interfaces, illustrating how rate-and-state friction phenomenology can predict system response. Case studies 2 and 3 probe rough interfaces directly to elucidate how the observed macroscale friction behavior links to the detailed behavior of contact junctions. Finally, in Case study 4, we present adhesion of soft elastomers in contact with rough low-energy diamond surfaces and how the elastic energy required to create conformal contact reduces adhesion.

condensation,¹⁴ and tribo-chemical reactions.^{15,16} Thus, the macroscopic behavior of a rough contact can be seen as a complex sum over the micro- or nano-junctions, the weights of which are nontrivial due to possible interactions between junctions. Such upscaling models exist,^{17–20} but no definitive way of upscaling the micro-junction behavior to that at the macroscale has yet been identified. Hence, the nanometer-scale knowledge provided about individual junctions for instance by the field of nanotribology,²¹ with dedicated experimental tools, remains insufficient to understand the behavior of extended rough contacts; therefore larger-scale, multi-contact experiments remain crucial in tribology.

The important key toward understanding macroscopic adhesion and friction is to measure the morphology of contact interfaces. Techniques such as frustrated total internal reflection,²² fluorescence,²³ optical imaging,^{2,24–26} and infrared sum-frequency-generation spectroscopy (SFG) in dry^{27–30} and wet environments^{31–34} are beginning to shed light on the contact morphology and in some cases during sliding and unloading in the presence of adhesion. In addition, the combination of surface characterization techniques such as transmission electron microscopy (TEM), atomic force microscopy (AFM), and optical/stylus profilometry are providing a complete characterization of the power spectral density (PSD) of surface topography over a broad wavelength range from the millimeter to the nanometer length scale.³⁵ The broad-spectrum measurement of the PSD has made it possible to directly compare models with experiments.

Experimental methods

In multi-contact tribology experiments, macroscopic interfaces are externally loaded with normal and tangential forces. This typically involves a system centered about a block-on-substrate interface as schematically illustrated in Figure 1. For friction measurements, the interface is loaded in the normal (F_N) and tangential (F_T) directions through springs that represent the normal (k_N) and tangential (k_T) stiffness of the measurement system. For adhesion measurements, only a normal, tensile, force (F_N) is applied. To avoid alignment difficulties, the block typically takes on a curvature resulting in a circular contact zone. The apparatus, the associated spring stiffnesses and the multi-contact interface control the system response, which is measured by a force-sensing method, as in, for example, References 36, 37. By applying suitable forces, velocities (v_T , v_N) or displacements, the pull-off (adhesion) forces and friction coefficient (the ratio of friction force to normal force) can be measured. If the springs are much stiffer than the interface, the interfacial stiffness can also be measured.

Importantly, in the last decades, the understanding of multi-contact friction and adhesion has been aided by additional *in situ/in operando* measurements of the spatial distributions and time dynamics of quantities such as contact area^{2,22–26} and morphology,^{2,23,24,26,38} the local interfacial gap,^{39,40} and the interfacial displacements and stresses.⁴¹ Such *in situ* measurements sometimes impose experimental constraints, for instance transparency or smoothness of one of the solids.

Case study 1: Rate-and-state friction in MEMS interfaces

In MEMS, polycrystalline silicon (polysilicon, a technical ceramic) is the most common structural material. Polysilicon contacts form opaque multi-contact interfaces. Calculations based on surface roughness measurements indicate that the asperities are subject to pressures approaching the hardness of silicon (~ 10 GPa⁴²), and hence the loading is elastoplastic.⁴³ The asperity junction contact diameters are on the order of 10 nm, making direct visualization of the interface difficult. Microinstruments co-fabricated adjacent to MEMS devices enable high-resolution tribological measurements. Although polysilicon is stiff (Young's modulus $E = 164$ GPa⁴⁴) and exhibits high tensile strength of 2–3 GPa,⁴⁵ it is brittle and forms a hydrophilic native oxide. As such, polysilicon interfaces exhibit high adhesion, friction, and wear. In the absence of hydrophobic coatings, the interface is easily filled by condensed water because MEMS surface roughness is small, typically just a few nanometers. This results in strong capillary forces that enormously increase adhesion.^{46–48} A common method to reduce susceptibility to these issues is to apply organic monolayer coatings through vapor^{49,50} or liquid⁵¹ processes. Such coatings reduce water adsorption, and liquid bridges do not form. The coatings also lower the shear strength between contacting asperities, and hence, lower friction and wear.

The rate-and-state friction framework incorporates the effects of time and velocity, and the associated propensity for stick–slip or steady sliding.^{52,53} It applies up to the scale of earthquakes^{54,55} and down to microscale contacts.⁵⁶ Two state variables, asperity contact time and block velocity (distinct from v_T when stick–slip occurs), and their interactions with k_T , F_N , and v_T , govern the system response. Parameters

known as the aging and velocity-strengthening coefficients must be measured to fully describe the system. Well-defined tests, including the ability to change v_T instantaneously, are needed to make these measurements.

Friction changes only gradually over decades of block velocity, but friction forces vary rapidly when transitioning from static to dynamic sliding. Inertial forces must then be taken into account as well. A stiff high-force actuator with a large v_T range is needed to test whether rate-and-state friction applies at any given scale. In MEMS, iterative learning control⁵⁷ can be applied to a stiff thermal actuator to control velocity more than 4.5 decades from 0.1 to 3000 $\mu\text{m/s}$, and velocity can be changed instantaneously by a factor of 20 using this method.⁵⁸

Typical MEMS tribometers, consisting of comb-drive actuators and a multi-contact interface,⁵⁹ have provided much useful information. One outstanding example is the ability of simple alcohols to form a protective layer via tribochemistry, essentially eliminating wear.⁶⁰ However, such tribometers are limited to a small range of F_T , and actuator velocity v_T is not well controlled. A MEMS tribometer suitable for the full array of required test types is shown in Figure 2a. There, a thermal actuator pulls on a spring which in turn pulls the friction block. The spring constant is varied from one device to another by changing its beam lengths. Electrostatic force is applied to some regions of the friction block to apply F_N , which is sustained at a frictional interface designed within it. The tests are run with computer control of thermal actuator signals and deflections are measured using a high-speed camera operating at up to 200,000 frames per second. Further details are given in Reference 61.

Figure 2b shows a resulting friction phase diagram. For example, with $k_T = 10$ N/m and constant thermal actuator velocity, v_T , the block experiences stick–slip at large F_N

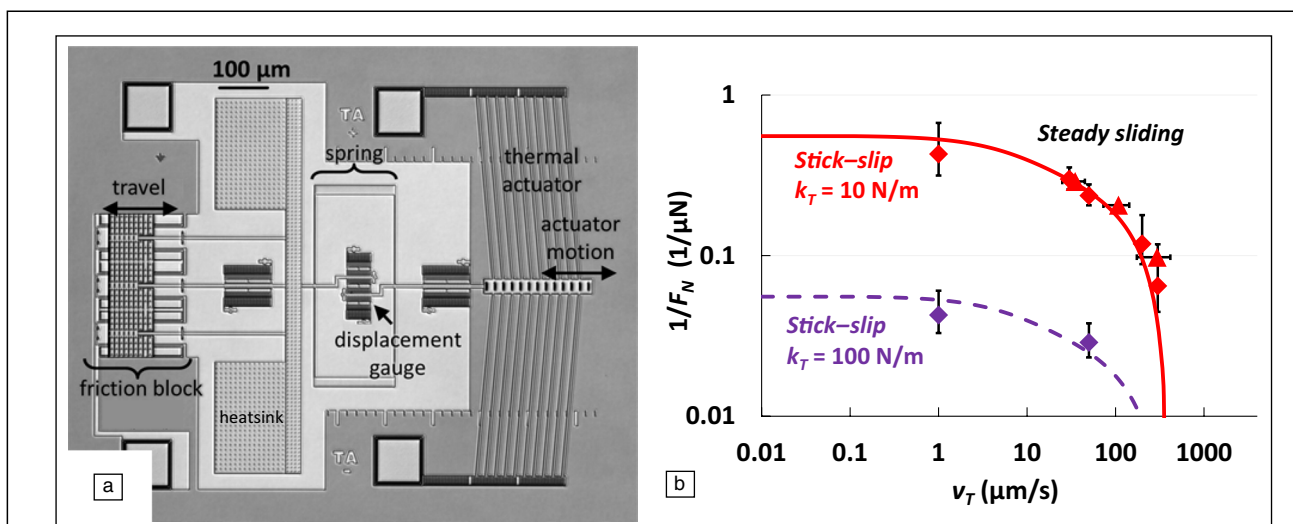


Figure 2. (a) Microscale implementation of Figure 1 designed to measure rate-and-state friction parameters. Key components include a thermal actuator (TA), a spring, and a friction block constituting the multi-contact interface. (b) Friction phase diagram. Solid and dashed lines show derived predictions for bifurcation from stick–slip to steady sliding based on rate-state parameters and perturbation theory. Data points indicate measured bifurcations, which occur by changing thermal actuator velocity v_T , or block normal load, F_N . Reprinted with permission from Reference 62.

(small $1/F_N$). As F_N decreases, the behavior transitions to steady sliding. If instead F_N is held constant but v_T increases, the behavior again transitions from stick–slip to steady sliding. Values of measured rate-and-state parameters from five different types of tests are combined as input to perturbation theory⁶² to derive the solid and dashed lines seen in Figure 2b. They predict the transition from stick–slip to steady sliding behavior for $k_T = 10$ and 100 N/m. The modeled lines are independently verified by direct testing. That is, the data markers in Figure 2b indicate observed experimental values of v_T and F_N at which these transitions occur, either through decreasing F_N or increasing v_T . It is seen that the markers well follow the lines predicted by perturbation theory.

Within the stick–slip region, state-space simulations capture the amplitude of the oscillations.⁶¹ Hence, with a well-designed *in operando* platform, many details of MEMS frictional behavior can be learned. It is verified that rate-and-state friction phenomenology extends from the scale of earthquake faults as formed by rock gouge to interfaces in MEMS as formed by collections of nanometer-scale junctions.

Case study 2: Evolution of the real contact area in an elastomer under shear

The generic character of friction phenomenology (i.e., rate-and-state friction) seen across many different systems and at different length scales is a strong motivator behind the detailed study of the interplay between the micro-junction response and macroscopic friction behavior in model systems. While the emergence of a collective behavior of micro-junctions cannot be directly observed in the case of MEMS, rough contact morphology can be monitored in the case of polymers, because their relatively small Young's modulus yields larger, more easily observable micro-junctions. Under pure normal load, polymer contact morphology can in particular be successfully related to the normal force, surface topography, elastic moduli, adhesion energy, or plastic yield stress.^{23,63} Recent experiments performed on elastomers (poly(dimethylsiloxane) (PDMS), $E = 1.6$ MPa) have shed light on the additional, unexpectedly large effect on contact morphology of a shear force applied on the interface.

Figure 3 shows a sketch of the rough elastomer/smooth-glass experiment (panel A) and a typical picture of the contact interface (panel B), where intimate contact zones appear as dark patches with dimensions on the order of 100 μm . Image analysis enables monitoring of the morphology of each individual micro-junction (inset of panel B), and its evolution as shear increases. The commonly accepted view is that the real contact area mainly depends on the normal load and age of the interface, so that the contact area would not change with shear loading and the interfacial shear stress would increase in direct proportionality with the tangential force. In contrast, the measurements reveal that the total contact area of the interface is, unexpectedly, a strongly decreasing function of the shear force.² In those conditions, the interfacial shear stress increases faster than expected

because the real contact area decreases at the same time as the tangential force increases. The area reduction is found to be quadratic with the shear force, with overall area reductions as large as 30% reached when the contact starts to slide. At that instant, the static friction force, $F_{T,s}$, is proportional to the concurrent contact area, A_s^R , through $F_{T,s} = \sigma_T A_s^R$, where σ_T is the interfacial friction strength. It has been further shown that the correlation lengths of the real contact evolve differently along directions parallel and perpendicular to the shear direction, indicating that an initially isotropic interface becomes more and more anisotropic as shear loading increases.³⁸ Those macroscopic observations demonstrate that the contact configuration at the onset of sliding is very different from that under pure normal loading, suggesting that the interface properties (see the “Introduction”) will also strongly evolve under shear.

Careful inspection of the contact images reveals that both area reduction and anisotropy growth originate at the micro-junction level (inset of panel B, Figure 3). This observation prompted complementary experiments on single sphere/plane contacts^{2,64} as proxies for individual micro-junctions, in order to identify the physical mechanisms underlying shear-induced morphology changes. The simple sphere/plane geometry enabled quantitative comparison with various models.^{64–67} Taken collectively, those comparisons demonstrate that two main ingredients contribute to morphology changes. First, due to the large ratio of friction stress at the interface to the elastomer's shear modulus, large strains develop and peel off the contact's trailing edge,⁶⁶ helping to explain the anisotropy. Second, due to adhesion, a stress concentration exists at the contact edge, leading to a crack-like motion of the edge, enabled by the macroscopic shear loading.⁶⁵ Although it is thought that adhesion and finite strains, respectively, dominate in contact under smaller and larger normal loads,⁶⁷ a clear description of the interplay between both effects is still lacking.

The rough-on-smooth contact case shown in Figure 3 is expected to involve the same two main ingredients, but with the additional complexity that, due to the random nature of the topography, each micro-junction is locally submitted to different normal and tangential loads. Although two models have attempted to reproduce shear-induced rough contact-area reduction,^{68,69} none has fully managed to quantitatively match the experiments of Reference 2. Future success will likely employ a numerical model incorporating roughness, friction, adhesion, and finite strains, but such a tool remains to be developed.

Case study 3: Capillary adhesion and friction at ceramic interfaces

Area-controlled friction, in which the friction force is proportional to the area of real contact, prevails at soft interfaces that experience strong adhesion and a relatively constant interfacial shear strength, such as the PDMS-on-glass contacts highlighted in Case study 2: $F_T = \sigma_T A_S^R$. (The subscript S in A_S^R

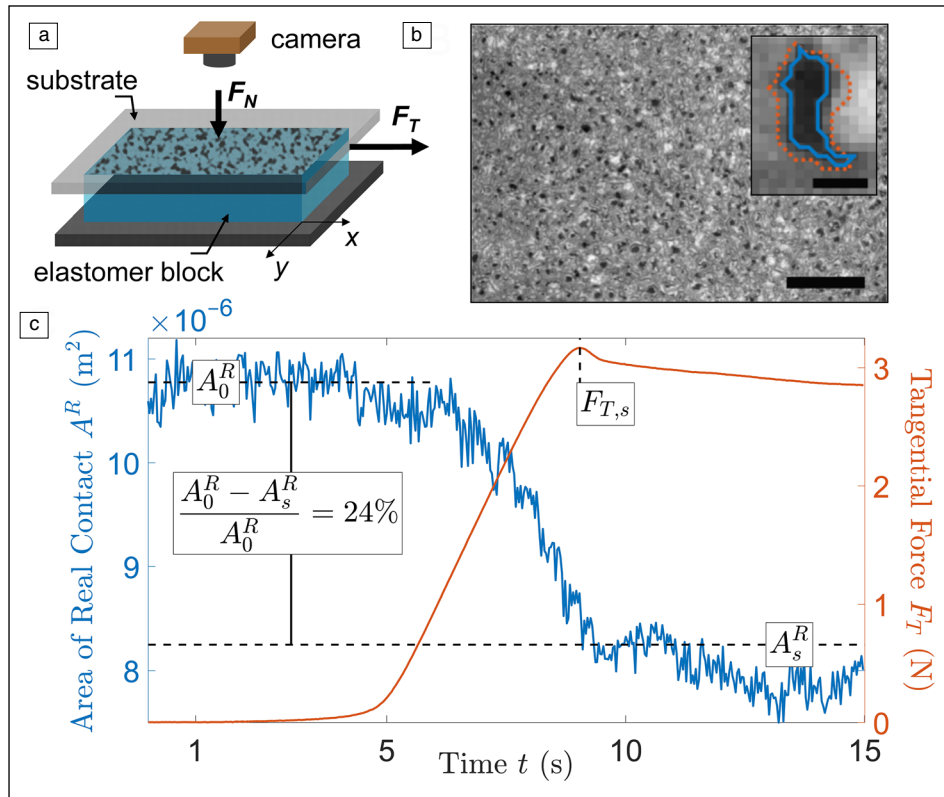


Figure 3. (a) Schematic representation of the experiment. (b) Typical image of a rough elastomer contact. Scale bar = 1.87 mm. Inset: Zoom-in on a micro-junction. Red designates the outer contour of this contact patch for $F_T = 0$; blue designates the contour of the same contact patch at $F_T = F_{T,s}$. Scale bar = 100 μm . (c) Typical concurrent evolution of the area of real contact (blue) and the tangential force (red), as a function of time. A_0^R : initial area. A_s^R : area at static friction $F_{T,s}$. Adapted from Reference 2.

indicates that the area is taken at the static friction peak [i.e., at its minimum in elastomer contacts]; see Case study 2. In the following, this subscript is dropped because the interfaces are stiffer, leading to negligible shear-induced contact shrinkages.⁷⁰ However, at interfaces between stiffer materials where the local contact pressures are high compared to the adhesive interactions, the interfacial shear strength, σ_T , is not necessarily constant and independent of the local normal stress, that is, $\sigma_T = \sigma_T(\sigma_N)$. In fact, it has been demonstrated⁷¹ that in so-called “load-controlled friction” the interfacial shear stress is proportional to the interfacial normal stress, $\sigma_T(\sigma_N) = \mu\sigma_N$, with μ the ratio of the friction force to the normal force, rendering the friction force independent of the area of real contact: $F_T = \sigma_T(\sigma_N)A^R = \mu\sigma_N F_N / \sigma_N = \mu F_N$. In other words, doubling the area of real contact while maintaining a constant normal force has no effect on the friction force in load-controlled friction. Experimentally observing load-controlled multi-contact interfaces is challenging, because stiff materials—as opposed to, for example, PDMS—yield small micro-junctions that are difficult to observe. Recent advances in *in situ* contact imaging have enabled direct observation of nanoscale multi-contact deformation through the use of fluorescence microscopy.^{40,72,73} This opens up the possibility of comparing model predictions

of the rough-contact formation process²⁰ to detailed experimental observations. These studies have shown that although complex plastic deformation needs to be taken into account to accurately describe the rough contact mechanics of plastics such as polystyrene and PMMA,²³ stiffer ceramic materials with high hardness follow linearly elastic multi-contact deformation behavior.⁷²

It is well known from analytical and numerical theory that for multi-contact interfaces governed by elastic deformations, the area of real contact is set by the surface topography: smoother surfaces create a larger area of real contact.⁷⁴ The friction generated at very smooth linearly elastic ceramic multi-contact interfaces was recently shown to be insensitive to the area of real contact (load controlled⁷²). The friction force scaled with the total repulsive force generated by the micro-contacts. For most

multi-contact interfaces, the total repulsive force generated by the micro-contacts is given by the externally applied normal load. However, for interfaces at which the surface roughness is so low that a significant fraction of the interface is separated by gaps of nanometer-scale (i.e., MEMS), adhesion becomes an additional contributor to the interface load.⁷⁵

Water capillary bridges, nucleated from ambient air or grown from pre-adsorbed water films on hydrophilic surfaces, can generate significant adhesion driven by the Laplace pressure difference between the inside and outside of the negatively curved capillaries.⁷⁶ This capillary adhesion was quantified in Reference 72 through a basic multi-contact model, based on equilibrium values for the range and strength of capillary adhesion. The model assumed that the friction force is increased due to capillary adhesion, simply because the capillary adhesion increases the total load while the load-controlled friction coefficient is constant. Impressively, such model predictions—without adjustable parameters—successfully capture how the macroscopic SiN-on-sapphire friction coefficient measured in an ambient environment increased with decreasing surface roughness due to capillary adhesion (Figure 4). This conclusion was supported by the experimental observation that the influence of capillary adhesion on the

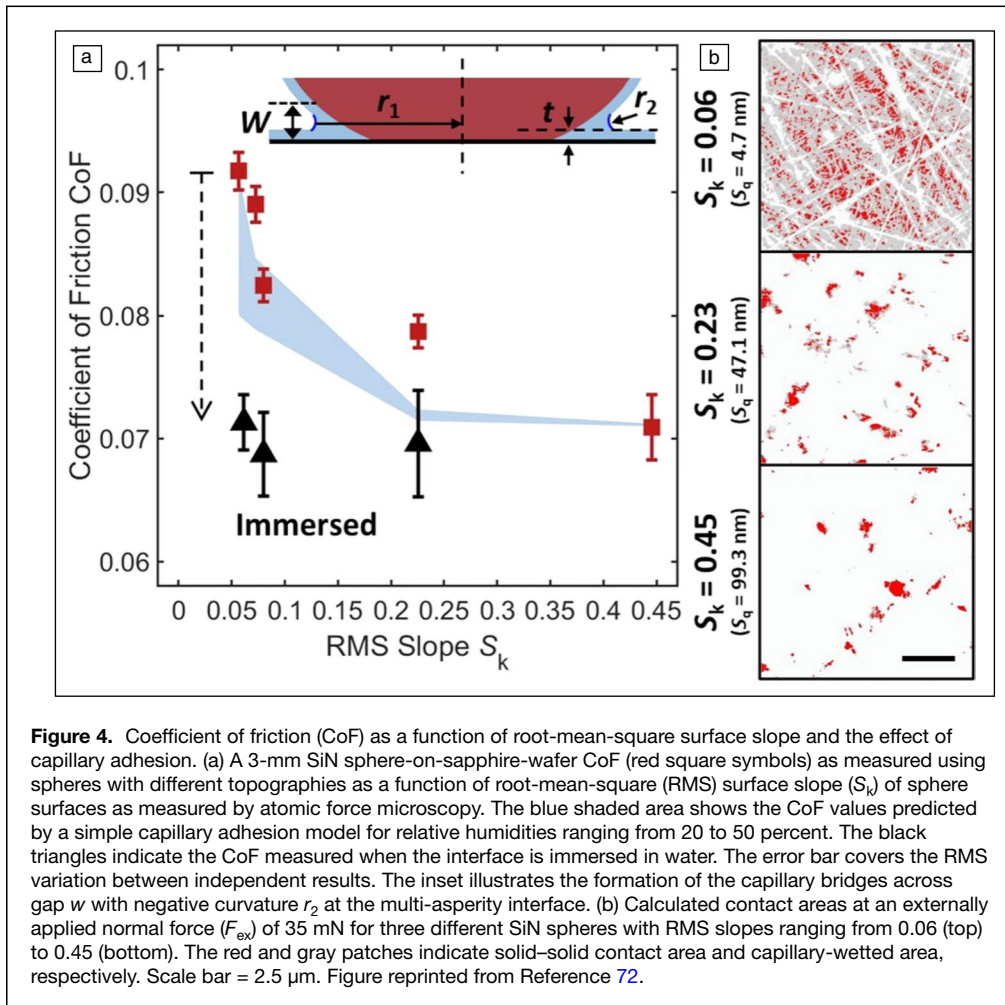


Figure 4. Coefficient of friction (CoF) as a function of root-mean-square surface slope and the effect of capillary adhesion. (a) A 3-mm SiN sphere-on-sapphire-wafer CoF (red square symbols) as measured using spheres with different topographies as a function of root-mean-square (RMS) surface slope (S_k) of sphere surfaces as measured by atomic force microscopy. The blue shaded area shows the CoF values predicted by a simple capillary adhesion model for relative humidities ranging from 20 to 50 percent. The black triangles indicate the CoF measured when the interface is immersed in water. The error bar covers the RMS variation between independent results. The inset illustrates the formation of the capillary bridges across gap w with negative curvature r_2 at the multi-asperity interface. (b) Calculated contact areas at an externally applied normal force (F_{ex}) of 35 mN for three different SiN spheres with RMS slopes ranging from 0.06 (top) to 0.45 (bottom). The red and gray patches indicate solid–solid contact area and capillary-wetted area, respectively. Scale bar = 2.5 μ m. Figure reprinted from Reference 72.

friction coefficient could be canceled by immersing the interface in liquid water, thereby avoiding the formation of water capillary bridges.

Case study 4: Soft elastomer adhesion

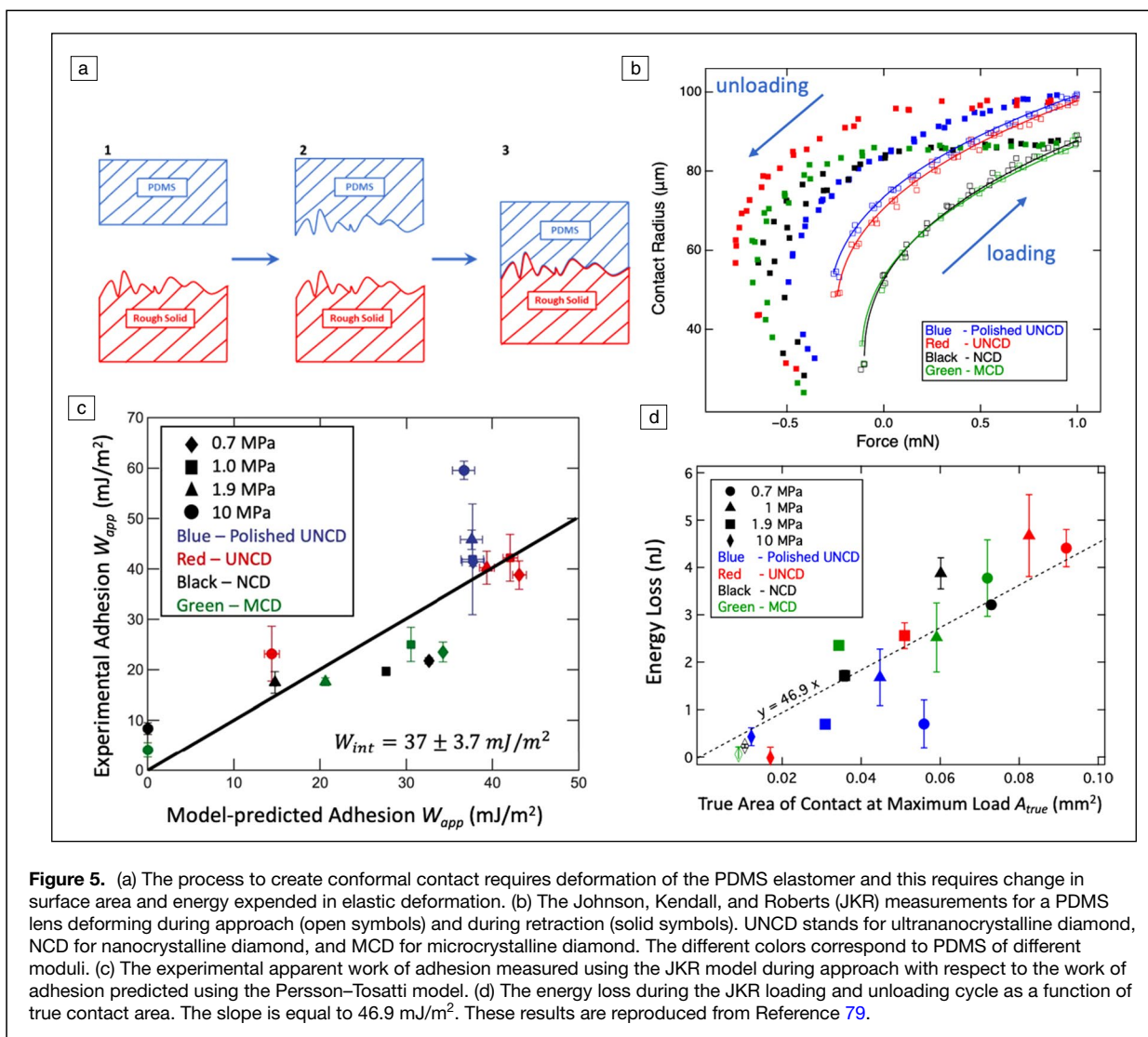
Increasing surface roughness can reduce adhesion at stiff ceramic interfaces, but may have the opposite effect at soft interfaces because soft materials can fully conform to the surface roughness creating an increased area of real contact. Soft elastomer adhesion is important for technological applications, including tires, biomedical adhesives/bandages, haptics, and soft robotics. A seminal paper by Johnson, Kendall, and Roberts (JKR) provided a formulation to explain the increase in contact area compared to a nonadhesive Hertzian model.⁷⁷ Roughness influences adhesion in two important ways. First, the adhesion can increase because the real contact area can be larger than the apparent contact area due to roughness. Second, adhesion can decrease due to the energy expended in creating conformal contact (Figure 5a). The Persson–Tosatti model predicts how elastic energy is determined using the power spectral density and the mechanical properties of the elastomer.⁷⁸ The Persson–Tosatti model was tested recently

by Dalvi et al.⁷⁹ using rough diamond nanocrystalline films in contact with poly(dimethylsiloxane) (PDMS) elastomers similar to those used in Case study 2. The experimental design incorporated low viscoelasticity elastomers to reduce viscous dissipation, included complete characterization of the PSD, and used surfaces with low surface energy so that the adhesion would be dominated by dispersion interactions.

Figure 5b shows the contact radius as a function of load during approach and retraction for four rough diamond surfaces using a PDMS hemispherical lens with 1.9 MPa modulus. The approach data (points shown with fitting curves) could be fitted using the JKR model (which itself does not account for surface roughness), but the predicted apparent work of adhesion from this fit is lower than that expected from the thermodynamic work of adhesion.

Interestingly, the retraction data show hysteresis that increases with roughness, and the results cannot be modeled using the JKR equation with a constant work of adhesion. Although this large hysteresis is typically attributed to viscoelasticity, this explanation does not apply here. This investigation used PDMS specifically because it has low viscoelasticity, and experiments were conducted at a low retraction velocity of 60 nm/s to reduce viscoelastic contributions. The apparent work of adhesion measured during approach is compared to predictions by the Persson–Tosatti model (Figure 5c). For this comparison, the Persson–Tosatti model was modified to include the increase in surface energy of PDMS to conform to the rough surfaces.⁷⁹ The predicted value of the thermodynamic work of adhesion is close to that expected for PDMS in contact with low-energy surfaces.

The retraction data show significant pinning (regions where the contact radius does not decrease during the unloading cycle, Figure 5b) and the force–displacement data were analyzed to calculate the energy loss as a function of actual contact area (Figure 5d). Interestingly, the slope in Figure 5d is close to the work of adhesion during approach that was obtained using the modified Persson–Tosatti



model. The validation of a Griffith-like model during retraction indicates that the stored elastic energy is dissipated in creating new surfaces. Dalvi et al.⁷⁹ used PDMS of moduli from 0.7 to 10 MPa and assumed conformal contact; this assumption is expected to be inapplicable for higher modulus materials, as the elastic energy to create conformal contact will exceed the energy gained by adhesion. For underwater adhesion, we expect that hydrodynamics will play an important role in restricting conformal contact, as water may remain trapped during evacuation.⁸⁰ In the future, understanding conformability and how these complex conditions influence actual contact will be important for understanding real-life problems.

Perspective

Understanding frictional instabilities has always been challenging and Case study 1 describes the influence of system parameters such as puller velocity, normal load, and apparatus stiffness on the transition from steady sliding to stick–slip sliding. The

observation that the rate-and-state friction phenomenology captures tribological behavior at both the scale of earthquakes and the scale of MEMS suggests the existence of underlying fundamental and generic friction mechanisms responsible for the behavior of micro- or nano-junctions. The main obstacle to understand the influence of roughness on adhesion and friction is the changes at the micro-/nano-junctions during loading, sliding, and aging, and how this controls the overall friction and adhesion. One approach toward exposing such mechanisms is to conduct model experiments on specific, well-chosen interfaces that have the potential to reveal how asperity junctions are deforming or interacting to define the system response, as shown in Case studies 2, 3, and 4. Case study 2 highlighted the fact that contact morphology at the onset of sliding may be very different than the contact morphology under purely normal loading. This points to the need to directly measure the contact interface during loading and sliding. This is even more important in the presence of humidity because it leads to capillary condensation and influences both adhesion and

friction (Case study 3). For soft contacts, the model proposed by Persson and Tosatti provides the necessary framework to understand the drop in adhesion due to elastic energy stored when creating a rough but conformal contact (Case study 4). An open question is whether a similar energetic approach could be used to understand friction observations on the same materials, like those of Case study 2. The friction for rough elastomeric sliding is complicated due to the influence of both the bulk viscoelastic properties and the energy spent in stretching of surface-attached polymer chains.^{81–86} This leads to complex dependence of friction on velocity and roughness, and requires rigorous experimental verifications of these models.⁸⁶

As powerful *in operando* visualization methods continue to evolve, more progress will be made in linking individual asperity deformations and their interactions to system response. Among the outstanding questions, addressable by careful experiments, are the following.

- What are the mechanisms underlying rate-and-state friction and are these mechanisms independent of the materials—for example, stiff silicon and compliant PDMS—or simply characterized by laws fortuitously having similar functional forms?
- How do the rate-and-state-friction parameters connect to the multiscale topography of the contacting topographies?
- How do friction and adhesion stresses couple, both at the single-asperity and at the macroscopic scale, especially when realistic, complex contact kinematics involving simultaneous variations of normal and tangential forces are involved?

Models, for example, Reference 87, address these questions as well. On the experimental side conceptual progress may be made thanks to the use of carefully designed, simplified rough surfaces, in which the spectral contents of the topography could be tuned, for instance by filtering out controlled amounts of the smallest wavelengths, those that are the hardest to accurately measure. This will progressively become a realistic strategy, thanks to progress in micro-/nanofabrication methods such as 3D printing, lithography, or laser texturing. Furthermore, by combining detailed measurement of specific randomly rough surfaces with adhesion and friction experiments, generic links between topography and mechanics can be exposed, as illustrated by Case studies 3 and 4. Furthermore, progress in theoretical descriptions⁸⁸ and industrial needs require the inclusion into this framework of wear,^{89–91} with its dynamically evolving surface topography. Future progress hinges on understanding the physio-chemical changes that may be taking place at asperity junctions and their relationship to friction for both hard- and soft-contact interfaces.

Acknowledgements

This work has partly been carried out at the Advanced Research Center for Nanolithography, a public-private partnership of the University of Amsterdam, the Vrije Universiteit

Amsterdam, the Dutch Research Council (NWO) and the semiconductor equipment manufacturer ASML. This work was supported by LABEX MANUTECH-SISE (ANR-10-LABX-0075) of Université de Lyon, within the program Investissements d'Avenir (ANR-11-IDEX-0007) operated by the French National Research Agency (ANR). JS is indebted to Institut Carnot Ingénierie@Lyon for support and funding. MdB acknowledges funding from the U.S. National Science Foundation Leading Engineering for America's Prosperity, Health, and Infrastructure (LEAP HI) Program under Grant CMMI-1854702. AD research was supported by NSF (DMR-2208464).

Data availability

Data sharing not applicable to this article as no data sets were generated or analyzed during the current study.

Conflict of interest

On behalf of all authors, the corresponding author states that there is no conflict of interest.

Open access

This article is licensed under a Creative Commons Attribution 4.0 International License, which permits use, sharing, adaptation, distribution and reproduction in any medium or format, as long as you give appropriate credit to the original author(s) and the source, provide a link to the Creative Commons license, and indicate if changes were made. The images or other third party material in this article are included in the article's Creative Commons license, unless indicated otherwise in a credit line to the material. If material is not included in the article's Creative Commons license and your intended use is not permitted by statutory regulation or exceeds the permitted use, you will need to obtain permission directly from the copyright holder. To view a copy of this license, visit <http://creativecommons.org/licenses/by/4.0/>.

References

1. J. Scheibert, S. Leurent, A. Prevost, G. Debrégeas, *Science* **323**, 1503 (2009)
2. R. Sahli, G. Pallares, C. Ducottet, I.E. Benli, S. Alkhrass, M. Guibert, J. Scheibert, *Proc. Natl. Acad. Sci. U.S.A.* **115**(3), 471 (2018)
3. M. Ayyildiz, M. Scaraggi, O. Sirin, C. Basdogan, B.N.J. Persson, *Proc. Natl. Acad. Sci. U.S.A.* **115**, 12668 (2018)
4. A. Basu, G.G. Adams, N.E. McGruer, *J. Micromech. Microeng.* **26**, 104004 (2016)
5. P. Stoyanov, R.R. Chromik, *Materials (Basel)* **10**(5), 550 (2017)
6. A.I. Vakis, V.A. Yastrebov, J. Scheibert, L. Nicola, D. Dini, C. Minfray, A. Almqvist, M. Paggi, S. Lee, G. Limbert, J.F. Molinari, G. Anciaux, R. Aghababaei, S. Echeverri Restrepo, A. Papangelo, A. Cammarata, P. Nicolini, C. Putignano, G. Carbone, S. Stupkiewicz, J. Lengiewicz, G. Costagliola, F. Bosia, R. Guarino, N.M. Pugno, M.H. Müser, M. Ciavarella, *Tribol. Int.* **125**, 169 (2018)
7. A. Tuononen, *Tribol. Int.* **69**, 70 (2014)
8. K. Autumn, A. Dittmore, D. Santos, M. Spenko, M. Cutkosky, *J. Exp. Biol.* **209**, 3569 (2006)
9. P.H. Niewiarowski, A.Y. Stark, A. Dhinojwala, *J. Exp. Biol.* **219**, 912 (2016)
10. G.A. Abers, P.E. van Keken, B.R. Hacker, *Nat. Geosci.* **10**, 333 (2017)
11. T. Baumberger, C. Caroli, *Adv. Phys.* **55**, 279 (2006)
12. L. Bureau, T. Baumberger, C. Caroli, *Eur. Phys. J. E* **8**, 331 (2002)
13. Q. Li, T.E. Tullis, D. Goldsby, R.W. Carpick, *Nature* **480**, 233 (2011)
14. B. Sung, J. Kim, C. Stambaugh, S.-J. Chang, W. Jhe, *Appl. Phys. Lett.* **103**, 213107 (2013)
15. V. Brand, M.S. Baker, M.P. de Boer, *Tribol. Lett.* **51**, 341 (2013)

16. A. Erdemir, O. Eryilmaz, S. Kim, *Surf. Coat. Technol.* **257**, 241 (2014)
17. J. Greenwood, J. Williamson, *Proc. R. Soc. Lond. A* **295**, 300 (1966)
18. K. Fuller, D. Tabor, *Proc. R. Soc. Lond. A* **345**, 327 (1975)
19. J.K. Trømborg, H.A. Sveinsson, J. Scheibert, K. Thøgersen, D.S. Amundsen, A. Malthe-Sørenssen, *Proc. Natl. Acad. Sci. U.S.A.* **111**, 8764 (2014)
20. M. Müser, L. Nicola, *MRS Bull.* **47**(12) (2022). <https://doi.org/10.1557/s43577-022-00468-2>
21. T.D. Jacobs, C. Greiner, K.J. Wahl, R.W. Carpick, *MRS Bull.* **44**(6), 478 (2019)
22. S. Rubinstein, M. Shay, G. Cohen, J. Fineberg, *Int. J. Fract.* **140**, 201 (2006)
23. B. Weber, T. Suhina, T. Junge, L. Pastewka, A. Brouwer, D. Bonn, *Nat. Commun.* **9**, 888 (2018)
24. B. Krick, J. Vail, B. Persson, W. Sawyer, *Tribol. Lett.* **45**, 185 (2012)
25. A. Ovcharenko, G. Halperin, I. Etsion, M. Varenberg, *Tribol. Lett.* **23**, 55 (2006)
26. J. Dieterich, B. Kilgore, *Pure Appl. Geophys.* **143**, 283 (1994)
27. S. Singla, D. Jain, C.M. Zoltowski, S. Volefi, A.Y. Stark, P. Niewiarowski, A. Dhinojwala, *Sci. Adv.* **7**, eabd9410 (2021)
28. B. Gaire, S. Singla, A. Dhinojwala, *Nanoscale* **13**, 8098 (2021)
29. K. Nanjundiah, A. Anish Kurian, S. Kaur, S. Singla, A. Dhinojwala, *Phys. Rev. Lett.* **122**, 128004 (2019)
30. A.P. Defante, A. Nyarko, S. Kaur, T.N. Burai, A. Dhinojwala, *Langmuir* **34**, 4084 (2018)
31. N. Dhopatkhar, A.P. Defante, A. Dhinojwala, *Sci. Adv.* **2**, e1600763 (2016)
32. K. Nanjundiah, P. Hsu, A. Dhinojwala, *J. Chem. Phys.* **30**, 024702 (2009)
33. B. Yurdumakan, K. Nanjundiah, G.P. Harp, A. Dhinojwala, *J. Phys. Chem. C* **111**, 960 (2007)
34. S. Kaur, A. Narayanan, S. Dalvi, Q. Liu, A. Joy, A. Dhinojwala, *ACS Cent. Sci.* **4**, 1420 (2018)
35. A. Gujrati, S.R. Khanal, L. Pastewka, T.D.B. Jacobs, *ACS Appl. Mater. Interfaces* **10**, 29169 (2018)
36. M. Guibert, C. Oliver, T. Durand, T. Le Mogne, A. Le Bot, D. Dalmas, J. Scheibert, J. Fontaine, *Rev. Sci. Instrum.* **92**, 085002 (2021)
37. C. Grégoire, B. Laulagnet, J. Perret-Liaudet, T. Durand, M. Collet, J. Scheibert, *Sens. Actuators A Phys.* **317**, 112478 (2021)
38. R. Sahli, G. Pallares, A. Papangelo, M. Ciavarella, C. Ducottet, N. Ponthus, J. Scheibert, *Phys. Rev. Lett.* **122**, 214301 (2019)
39. A. Bennett, S. Rohde, K. Harris, K. Schulze, J.M. Uruëña, A.A. Pitenis, P. Ifju, T. Angelini, M. Müser, W. Sawyer, *Tribol. Lett.* **65**, 123 (2017)
40. D. Petrova, B. Weber, C. Allain, P. Audebert, D. Bonn, A.M. Brouwer, *ACS Appl. Mater. Interfaces* **10**, 40973 (2018)
41. A. Prevost, J. Scheibert, G. Debrégeas, *Eur. Phys. J. E* **36**, 17 (2013)
42. L.J. Vandeperre, F. Giuliani, S.J. Lloyd, W.J. Clegg, *Acta Mater.* **55**, 6307 (2007)
43. M.P. de Boer, D.L. Luck, W.R. Ashurst, A.D. Corwin, J.A. Walraven, J.M. Redmond, *J. Microelectromech. Syst.* **13**, 63 (2004)
44. B.D. Jensen, M.P. de Boer, N.D. Masters, F. Bitsie, D.A. LaVan, *J. Microelectromech. Syst.* **10**, 336 (2001)
45. M.E. Saleh, J.L. Beuth, M.P. de Boer, *J. Colloid Interface Sci.* **311**, 171 (2007)
46. M.P. de Boer, P.C.T. de Boer, *J. Colloid Interface Sci.* **311**, 171 (2007)
47. E. Soylemez, M.P. de Boer, *Langmuir* **30**, 11625 (2014)
48. E. Soylemez, M.P. de Boer, *Tribol. Lett.* **59**(5), 12 (2015)
49. T.M. Mayer, M.P. de Boer, N.D. Shinn, P.J. Clews, T.A. Michalske, *J. Vac. Sci. Technol. B* **18**, 2433 (2000)
50. W.R. Ashurst, C. Carraro, R. Maboudian, *IEEE Trans. Device Mater. Reliab.* **3**, 173 (2003)
51. U. Srinivasan, M.R. Houston, R.T. Howe, R. Maboudian, *J. Microelectromech. Syst.* **7**, 252 (1998)
52. J. Rice, A. Ruina, *J. Appl. Mech.* **50**, 343 (1983)
53. A.L. Ruina, *J. Geophys. Res.* **88**, 359 (1983)
54. J.H. Dieterich, *J. Geophys. Res.* **84**, 2161 (1979)
55. J.H. Dieterich, *J. Geophys. Res.* **84**, 2169 (1979)
56. F. Heslot, T. Baumberger, B. Perrin, B. Caroli, C. Caroli, *Phys. Rev. E* **49**, 4973 (1994)
57. D.A. Bristow, M. Tharayil, A.G. Alleyne, *IEEE Control Syst.* **26**(3), 96 (2006)
58. S.S. Shroff, M.P. de Boer, *J. Microelectromech. Syst.* **24**(6), 1868 (2015)
59. D. Berman, J. Krim, *Prog. Surf. Sci.* **88**, 171 (2013)
60. D.B. Asay, M.T. Dugger, J.A. Ohlhausen, S.H. Kim, *Langmuir* **24**, 155 (2008)
61. S.S. Shroff, M.P. de Boer, *Tribol. Lett.* **63**, 12 (2016)
62. S.S. Shroff, M.P. de Boer, *Tribol. Lett.* **63**, 15 (2016)
63. A. Bennett, K. Harris, K. Schulze, J. Uruëña, A. McGhee, A. Pitenis, M. Müser, T. Angelini, W. Sawyer, *Tribol. Lett.* **65**, 134 (2017)
64. J.C. Mergel, R. Sahli, J. Scheibert, R.A. Sauer, *J. Adhes.* **95**(12), 1101 (2019)
65. A. Papangelo, J. Scheibert, R. Sahli, G. Pallares, M. Ciavarella, *Phys. Rev. E* **99**, 053005 (2019)
66. J. Lengiewicz, M. de Souza, M.A. Lahmar, C. Courbon, D. Dalmas, S. Stupkiewicz, J. Scheibert, *J. Mech. Phys. Solids* **143**, 104056 (2020)
67. J. C. Mergel, J. Scheibert, R. Sauer, *J. Mech. Phys. Solids* **146**, 104194 (2021)
68. J. Scheibert, R. Sahli, M. Peyrard, *Front. Mech. Eng.* **6**, 18 (2020)
69. Y. Xu, J. Scheibert, N. Gadegaard, D. Mulvihill, *J. Mech. Phys. Solids* **164**, 104878 (2022)
70. B. Weber, T. Suhina, A.M. Brouwer, D. Bonn, *Sci. Adv.* **5**, eaav7603 (2019)
71. A. Berman, C. Drummond, J. Israelachvili, *Tribol. Lett.* **4**, 95 (1998)
72. F.-C. Hsia, S. Franklin, P. Audebert, A.M. Brouwer, D. Bonn, B. Weber, *Phys. Rev. Res.* **3**, 043204 (2021)
73. D. Petrova, B. Weber, C. Allain, P. Audebert, C.H. Venner, A.M. Brouwer, D. Bonn, *Sci. Adv.* **5**, 4761 (2019)
74. M.H. Müser, W.B. Dapp, R. Bugnicourt, P. Sainsot, N. Lesaffre, T.A. Lubrecht, B.N.J. Persson, K. Harris, A. Bennett, K. Schulze, S. Rohde, P. Ifju, W.G. Sawyer, T. Angelini, H.A. Esfahani, M. Kadkhodaei, S. Akbarzadeh, J.-J. Wu, G. Vorlauffer, A. Vernes, S. Solh-joo, A.I. Vakis, R.L. Jackson, Y. Xu, J. Strator, A. Rostami, D. Dini, S. Medina, G. Carbone, F. Bottogliione, L. Afferrante, J. Monti, L. Pastewka, M.O. Robbins, J.A. Greenwood, *Tribol. Lett.* **65**, 118 (2017)
75. A.D. Corwin, M.P. de Boer, *Appl. Phys. Lett.* **84**, 2451 (2004)
76. E. Soylemez, M.P. de Boer, *J. Micromech. Microeng.* **27**, 125023 (2017)
77. K. Johnson, K. Kendall, A.D. Roberts, *Proc. R. Soc. Lond. A* **324**, 301 (1971)
78. B.N.J. Persson, E. Tosatti, *J. Chem. Phys.* **115**, 5597 (2001)
79. S. Dalvi, A. Gujrati, S.R. Khanal, L. Pastewka, A. Dhinojwala, T.D.B. Jacobs, *Proc. Natl. Acad. Sci. U.S.A.* **116**, 25484 (2019)
80. M. Sun, N. Kumar, A. Dhinojwala, H. King, *Proc. Natl. Acad. Sci. U.S.A.* **118**, e2104975118 (2021)
81. B.N.J. Persson, *J. Chem. Phys.* **115**, 3840 (2001)
82. A. Tiwari, N. Miyashita, N. Espallargas, B.N.J. Persson, *J. Chem. Phys.* **148**, 224701 (2018)
83. A. Schallamach, *Proc. Phys. Soc. Sect. B* **66**, 386 (1953)
84. Y. Chernyak, A. Leonov, *Wear* **108**, 105 (1986)
85. K.A. Grosch, *Proc. R. Soc. Lond. A* **274**, 21 (1963)
86. D. Maksudata, S. Dalvi, A. Gujrati, L. Pastewka, T.D.B. Jacobs, A. Dhinojwala, *Soft Matter* **18**, 5843 (2022)
87. Y. Bar-Sinai, R. Spatschek, E.A. Brener, E. Bouchbinder, *J. Geophys. Res. Solid Earth* **119**(3), 1738 (2014)
88. S. Pham-Ba, J.-F. Molinari, *Tribol. Lett.* **69**, 107 (2021)
89. P. Spijker, G. Anciaux, J.-F. Molinari, *Tribol. Lett.* **44**, 279 (2011)
90. C. Leriche, S. Franklin, B. Weber, *Wear* **498**, 204284 (2022)
91. F.-C. Hsia, C.-C. Hsu, L. Peng, F.M. Elam, C. Xiao, S.E. Franklin, D. Bonn, B. Weber, *Phys. Rev. Appl.* **17**, 034034 (2022) □

Publisher's note

Springer Nature remains neutral with regard to jurisdictional claims in published maps and institutional affiliations.



Bart Weber leads the Contact Dynamics Group at the Advanced Research Center for Nanolithography and is appointed as a tenure track assistant professor at the University of Amsterdam, The Netherlands. His research covers the interplay between water and friction on granular materials, the slipperiness of ice and visualizing rough surface contact mechanics, and friction using fluorescent probe molecules. Currently, he is studying how wear and adhesion influence the friction behavior of stiff materials in the context of precision positioning. Weber can be reached by email at b.weber@arcn.nl.



Julien Scheibert has been a CNRS researcher since 2011. His research topics lie at the interface between physics and mechanics. He uncovered the role of fingerprints in the perception of fine textures by humans. He also investigated the fast rupture of brittle heterogeneous solids. Currently, Scheibert's main focus is on the contact mechanics, friction, and adhesion of interfaces between rough solids, using both experimental and numerical tools. He also develops metamaterials with controlled frictional properties. Scheibert can be reached by email at julien.scheibert@cnr.fr.



Maarten P. de Boer is a professor of mechanical engineering at Carnegie Mellon University. In research, his group designs, fabricates, and tests micromachined devices to measure mechanical and surface properties of thin films. He has published more than 100 archival journal and conference papers in these areas. De Boer can be reached by email at mpdebo@andrew.cmu.edu.



Ali Dhinojwala joined The University of Akron (UA) in 1997 in the Department of Polymer Science. He received his undergraduate degree in chemical engineering from the Indian Institute of Technology, India, and PhD degree from Northwestern University. After a two-year research scientist position at the University of Illinois at Urbana-Champaign and one year at GE Plastics, he joined UA in 1997, and has held administrative roles as a chair, dean, and a director of the Polymer Program at UA. His research interests focus on adhesion, friction, and wetting. Dhinojwala can be reached by email at ali4@uakron.edu.